All-fiber fully controlled Lyot filter based on bend-induced linear birefringence with tension

I. Armas-Rivera[a], L. A. Rodríguez-Morales[b], S. Cortés-López[c], M. Durán-Sánchez[a], M. V. Andrés[d], and B. Ibarra-Escamilla[a,*]

[a]Instituto Nacional de Astrofísica, Óptica y Electrónica (INAOE), Luis Enrique Erro 1, Sta. Ma. Tonantzintla, Puebla 72824, Mexico
[b]Centro de Investigaciones en Óptica (CIO), Loma del Bosque No. 115, Col. Lomas del Campestre, León, Guanajuato 37150, Mexico
[c]Tecnológico Nacional de México/ITS de Poza Rica, Luis Donaldo Colosio Murrieta S/N, Arroyo del Maíz, Poza Rica 93230, Mexico
[d]Departamento de Física Aplicada y Electromagnetismo, ICMUV, Universidad de Valencia, C/Dr. Moliner, 50, 46100 Burjassot, Spain

*corresponding author
email: baldemar@inaoep.mx

Abstract

In this work, we present a single-mode fiber fully controlled Lyot filter based on bend-induced linear birefringence with tension. The filter consists of 22.6 m of standard fiber coiled onto a 1.8792 cm radius cylinder. By increasing the fiber strain, the filter period can be dynamically varied from 70 to 30 nm. Also, the filter can be continuously tuned by adjusting the retardance of a variable wave retarder and in modulation depth from 0 to 1. The experimental results are supported by numerical simulations based on the Jones matrix formulation.
Keywords: Lyot filter, bend-induce linear birefringence, bend-induce linear birefringence with tension

1. Introduction

All-fiber technology is highly desirable in many industrial applications and scientific research due to its numerous advantages such as compactness, low cost, free of alignment, and high stability [1, 2]. Particularly, several applications such as sensors [2], imaging [3], optical communications [4], and continuous [5] and pulsed [6] tunable fiber lasers have the need to control the spectral width and to tune the central wavelength independently to improve its versatility and performance. To achieve it, several wavelength filter types such as fiber Bragg gratings (FBG) [7], interferometer filters [6], and birefringent fiber filters [8-11] have been proposed. The latter offers some advantages over the previous ones since are easy to fabricate and implement. The Lyot filter (LF) is a type of birefringent filter whose simplest implementation consists of a highly birefringent element inserted between two polarizers to induce wavelength-dependent modulation [11, 12]. In optical fiber, the LF is usually implemented with polarization-maintaining fiber (PMF), since it is a highly birefringent element whose birefringence can be varied by temperature or strain [13]. The LF has been numerically and experimentally investigated to enhance its performance and tunability; however, the improvement characteristics are usually independent or range-limited [14, 15]. Zhu et al. [16] demonstrate an ultra-broad period bend-induced birefringent LF by coiling 25-m of single-mode fiber (SMF-28) onto a 6.5 cm radius cylinder. By means of polarization controllers (PC), the LF shows different slope and amplitude transmission as gain-tilt spectral equalizers to balance an Erbium-doped fiber gain spectrum. Later [17], he proposed a constant period LF which can be dynamically tuned 30 nm by adjusting the PC, however, the modulation depth did not remain constant during tuning. Ding et al. [18] reported a LF built with a variable wave retarder (VWR) and a segment of PMF. The LF was continuously tuned 13.9 nm between 1036.6 and 1050.5 nm and in modulation depth in a controlled manner, nevertheless, no experimental or numerical details were given. Recently, Han et al. [19] reported a wavelength variable and tunable LF by inserting a piece of single-mode fiber between two PMFs acting as PC. The LF period can be varied from 5.9 to 14.5 nm and the central wavelength can be tuned 32 nm. And Dai et al. [20] have demonstrated a 28 nm wavelength-tunable, Er-doped mode-locked fiber, using a thermal-sensitive reflective Lyot filter.

In this work, we numerically and experimentally demonstrate a fully controlled LF based on bend-induced linear birefringence in a tension-coiled length of fiber. Increasing the strain of a 22.6 m of SMF-28 coiled onto a 1.8792 cm radius cylinder allows the filter period to be dynamically varied from 70 to 30 nm. Also, the filter can be continuously tuned by adjusting the retardance of a VWR and in modulation depth from 0 to 1 by varying the angle of an azimuth rotator. The experimental results were supported by numerical simulations based on the Jones matrix formulation.

2. Experimental setup and numerical model

The experimental setup is shown in Fig. 1. It consists of a depolarized continuous-wave erbium-doped fiber broadband source (BS, 1510 - 1580 nm) and a LF. The LF includes a first polarized beam splitter 1 (PBS-1), a VWR, 22.6 m of SMF-28, and a second PBS-2. The BS was connected to the PBS-1 SMF-28 port, acting as a linear polarizer. When incident light with any polarization state enters from the PBS-1 SMF-28 port, only one linearly polarized component passes through the PBS-1 Hi-Bi fiber port 1, while the other linearly polarized component passes through the Hi-Bi fiber port 2. The PBS-1 Hi-Bi fiber port 1 was used as Output-1 and connected directly to an optical spectrum analyzer (OSA, Anritsu MS9740A) to measure the input spectrum, while the PBS-1 Hi-Bi fiber port 2 was spliced (splice 1) to a 22.6 m SMF-28 coiled onto a cylinder of radius $R_0 = 1.8792\ cm$ (red cylinder) which was increased mechanically up to $R_1 = 1.8938\ cm$ (black cylinder). After splice 1, a VWR was inserted to induce linear birefringence by pressure [21]. The fiber was coiled barely tight by a mechanized method to avoid additional tension. In addition, the coiling process and the measurements were carried out at a constant temperature of 22 °C to avoid any thermal contributions. The SMF-28 output was then spliced (splice 2) to a PBS-2 Hi-Bi port, acting as a second linear polarizer. The output spectrum was measured by the OSA through Output-2. The LF transmission was calculated as the ratio between the output spectrum measured at Output-2 and the input spectrum measured at Output-1. For better experimental and numerical transmission comparison, the experimental transmission was normalized to the maximum value.

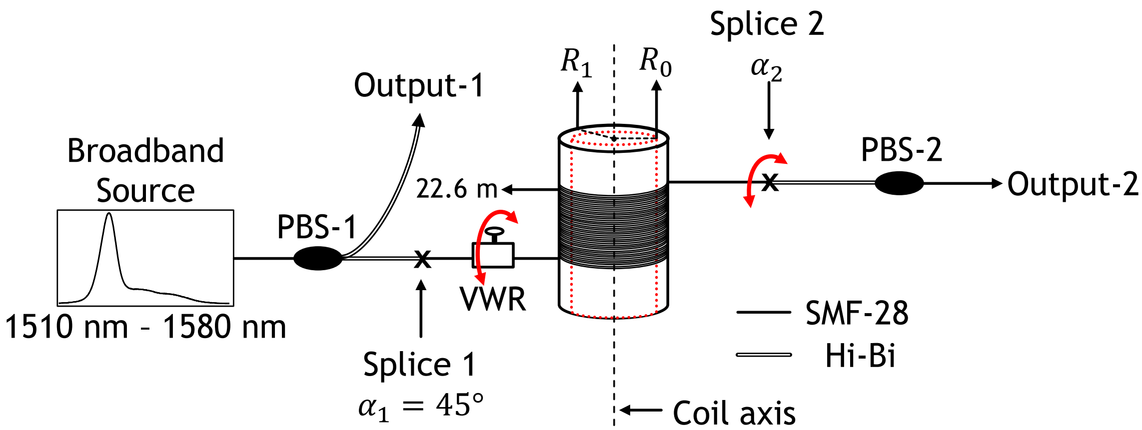

Fig. 1. Experimental setup.

In order to explain the LF behavior, we carry out some numerical simulations based on the Jones matrix formulation. The numerical model includes 22.6 m of SMF-28 in which linear birefringence was induced by bending and tension. The bend-induce linear birefringence β_c is given by Eq. 1 [22]:

$$\beta_c = \frac{1}{4}\kappa n^3 (p_{11} - p_{12})(1+v)K^2 r^2, \qquad \text{Eq. 1}$$

where $\kappa = 2\pi/\lambda_0$ is the wave number and λ_0 is the wavelength in vacuum, n is the refractive index, p_{11} and p_{12} are the strain-optical coefficients, v is the Poisson ratio, $K = 1/R$ is the cylinder curvature of radius R, and r is the fiber radius. The induced birefringence axes automatically align with the fast axis coinciding with the radius of curvature and the slow axis with the coil axis [22].

With the fiber coiled onto the cylinder, we increase the radius from R_0 to R_1, producing fiber lateral stress that induces an additional linear birefringence by tension β_{tc} given by [23]:

$$\beta_{tc} = \frac{1}{2}\kappa n^3 (p_{11} - p_{12})(1+v)(2-3v)(1-v)^{-1} K r \frac{\varepsilon_z}{2\pi}, \qquad \text{Eq. 2}$$

which is proportional to the fiber strain ε_z determined by the cylinder radius increase.

In a tension-coiled fiber, the principal axes also automatically align to the coil axis with the fast axis coinciding with the radius of curvature and the slow axis with the coil axis for both contributions, thus β_c and β_{tc} adds constructively as $\beta_{lin} = \beta_c + \beta_{tc}$ [23].

The LF transmitted field E_T was calculated as the product of matrices corresponding to all the elements given by Eq. 3:

$$E_T = M3 \cdot M2 \cdot M1 \cdot E_{in}, \qquad \text{Eq. 3}$$

where $E_{in} = \frac{1}{\sqrt{2}}\begin{bmatrix}1\\1\end{bmatrix}$ corresponds to a linearly polarized input field at $\alpha_1 = 45°$ respect to the radius of curvature, $M1 = \begin{bmatrix} e^{-i\frac{\delta_{l1}}{2}} & 0 \\ 0 & e^{i\frac{\delta_{l1}}{2}} \end{bmatrix}$ represents a fiber VWR under pressure [21, 24] with total retardance $\delta_{l1} = q\,\pi/2$ at 1550 nm (with $q = -2, -1, 0, 1, 2$) and birefringent axes aligned in the x and y coordinates –i. e., the fast and slow birefringent axes of the LF–, $M2$ describes the associated fiber matrix of length L_0 in which it is possible to induce linear β_{lin} and circular β_{cir} birefringence. Since the experimental setup is twist free, the fiber was modeled with $\beta_{cir} = 0$ and β_{lin} was modeled as a tension-coiled fiber, therefore, the total linear retardance is given by $\delta_{l2} = \beta_{lin} L_0$. Under these considerations, $M2 = \begin{bmatrix} e^{-i\frac{\delta_{l2}}{2}} & 0 \\ 0 & e^{i\frac{\delta_{l2}}{2}} \end{bmatrix}$, so the tension-coiled fiber fast axis coincides with the radius of curvature. Finally, $M3 = \begin{bmatrix} cos^2(\alpha_2) & \cos(\alpha_2)\, sin(\alpha_2) \\ \cos(\alpha_2)\, sin(\alpha_2) & sin^2(\alpha_2) \end{bmatrix}$ represents a linear polarizer at an angle α_2 with respect to the radius of curvature. The transmission was calculated as Eq. 4:

$$Trans = \frac{|E_T|^2}{|E_{in}|^2}. \quad \text{Eq. 4}$$

The values used in the numerical simulations were: $n = 1.46$, $(p_{11} - p_{12}) = -0.14$ [25], $v = 0.17$ [26], $r = 62.5\ \mu m$, $\alpha_1 = 45°$, and $\alpha_2 = 0°\ to\ -45\ °$ with 9° steps. The cylinder radius was changed from $R_0 = 1.8792\ cm$ to $R_1 = 1.8938\ cm$ with $5.8x10^{-4}\ cm$ steps, corresponding to a fiber length and a fiber strain variation of $L_0 = 22.6\ to\ 22.7755\ m$ with $7.0234x10^{-3}\ m$ steps and $\varepsilon_z = 0\ to\ 7.7692x10^{-3}$ with $3.1077x10^{-4}$ steps, respectively.

To show that the LF period can be varied by increasing ε_z from 0 ($R_0 = 1.8792\ cm$) to $7.7692x10^{-3}$ ($R_1 = 1.8938\ cm$), we perform the numerical simulation for $L_0 = 12.6\ m$ (blue line), $L_0 = 22.6\ m$ (black line), and $L_0 = 32.6\ m$ (red line) and were plotted in Fig. 2. This figure shows that the period can be varied continuously from 125.05 to 54.94 nm, 69.72 to 30.63 nm, and 48.33 to 21.23 nm for 12.6, 22.6, and 32.6 m, respectively.

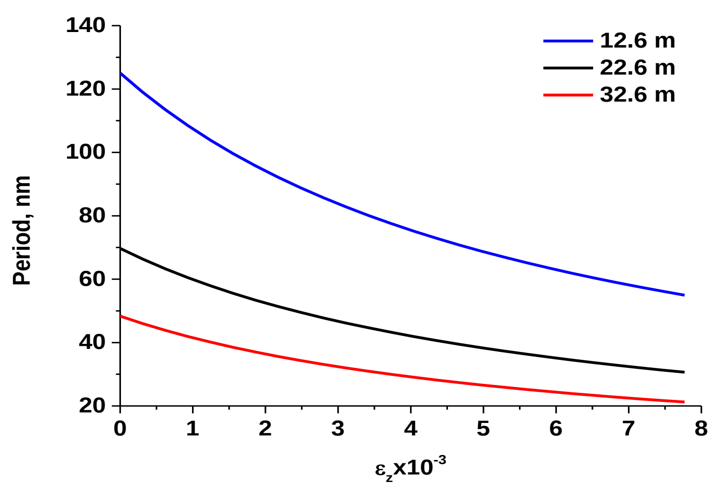

Fig. 2. LF period for $L_0 = 12.6\ m$ (blue line), $L_0 = 22.6\ m$ (black line), and $L_0 = 32.6\ m$ (red line) increasing ε_z from 0 ($R_0 = 1.8792\ cm$) to $7.7692x10^{-3}$ ($R_1 = 1.8938\ cm$).

For the following experimental results and numerical simulations, we choose 22.6 m since it better fits the used BS bandwidth.

3. Results and discussions

Experimentally, we first set $\alpha_1 = 45°$, $\alpha_2 = -45°$, and $\delta_{l1} = 0$. During all measurements, α_1 was fix to this angle value. At an initial radius R_0; $L_0 = 22.6\ m$, $\varepsilon_z = 0$, and $\beta_{tc} = 0$. Then, we measure the LF transmission and plot it in Fig 3. The measured LF period was 70 nm (blue dotted line). Afterwards, we increase the cylinder radius mechanically to $R_1 = 1.8807, 1.8885, and\ 1.8938\ cm$ and the measured LF transmissions were also plotted in Fig. 3 with measured periods of 52 nm (black dotted line), 45 nm (red dotted line), and 30 nm (magenta dotted line), respectively. Also, Fig. 3 shows the numerical simulations with the same periods for $R_0 = 1.8792\ cm$ (70 nm, blue solid line), $R_1 = 1.8832\ cm$ (52 nm, black solid line), $1.8856\ cm$ (45 nm, red solid line), and $1.8938\ cm$ (30 nm, magenta solid line). The small disagreements between the experimental and numerical radii values were due to experimental uncertainties in the small step increments between each measurement. The total radius change was 146 µm.

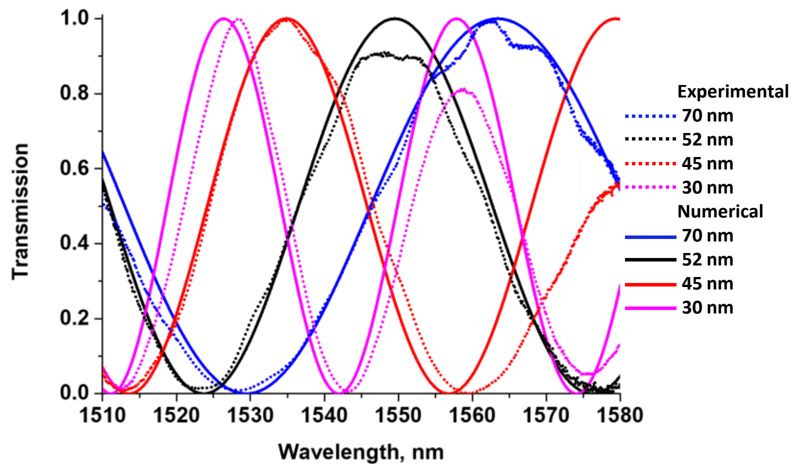

Fig. 3. Experimental (dotted lines) and numerical (solid lines) LF transmission for 70 nm (blue), 52 nm (black), 45 nm (red), and 30 nm (magenta) increasing ε_z from 0 ($R_0 = 1.8792\ cm$) to $7.7692x10^{-3}$ ($R_1 = 1.8938\ cm$).

Figure 4a shows the experimental (red squares) and numerical (black line extracted from Fig. 2) LF periods for ε_z from 0 ($R_0 = 1.8792\ cm$) to $7.7692x10^{-3}$ ($R_1 = 1.8938\ cm$). This figure shows that the experimental measurements and the numerical simulations are in agreement. For the same measurements, we determine the maximum transmission and show it in Fig. 4b. For these ε_z values, the maximum transmission remains almost constant at 0.5. We attribute the 3 dB losses to two factors: 1) the fiber coil has intrinsic losses due to bending with a relatively small radius and the fiber length [27], and 2) insertion losses due to PMF-SMF splices.

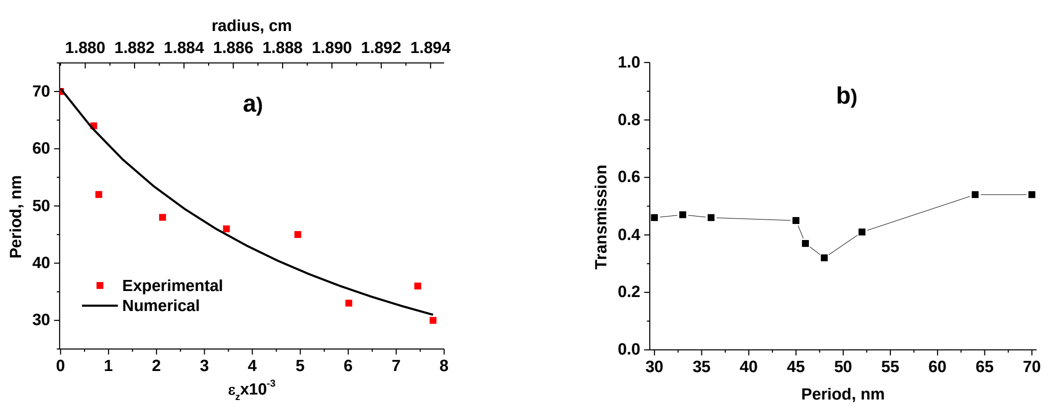

Fig. 4. a) LF periods for ε_z from 0 ($R_0 = 1.8792\ cm$) to $7.7692x10^{-3}$ ($R_1 = 1.8938\ cm$) for experimental (red squares) and numerical (black line), respectively and b) experimental maximum transmissions for the same LF periods.

The LF can be continuously tuned for a full wavelength period by changing δ_{l1} from $-\pi$ to π, by means of the VWR, independently of the period. Figure 5 shows a series of measurements for $R_0 = 1.8792\ cm$ (70 nm, Fig. 5a), $R_1 = 1.8885\ cm$ (45 nm, Fig. 5b), and $1.8938\ cm$ (30 nm, Fig. 5c) periods where the minimum transmission was tuned from 1515 to 1584.38 nm, 1526.39 to 1571.36 nm, and 1535.46 to 1565.48 nm, respectively. Since the VWR can only increase δ_{l1}, first we oriented the VWR at 90° with respect to the coil axis and then increase δ_{l1} from 0 to $\sim\pi$ at 1550 nm (red, black and blue dotted lines). Since the fast axis of the tension-coiled fiber and the VWR were first oriented orthogonal between each other, the birefringences adds destructively, $\delta_{l2} - \delta_{l1}$, so the spectrum blue-shifts. Then we orient the VWR at 0° and increase δ_{l1} from 0 to $\sim\pi$ at 1550 nm (magenta and cyan dotted lines) and the birefringences then adds constructively; $\delta_{l2} + \delta_{l1}$ so the spectrum red-shifts.

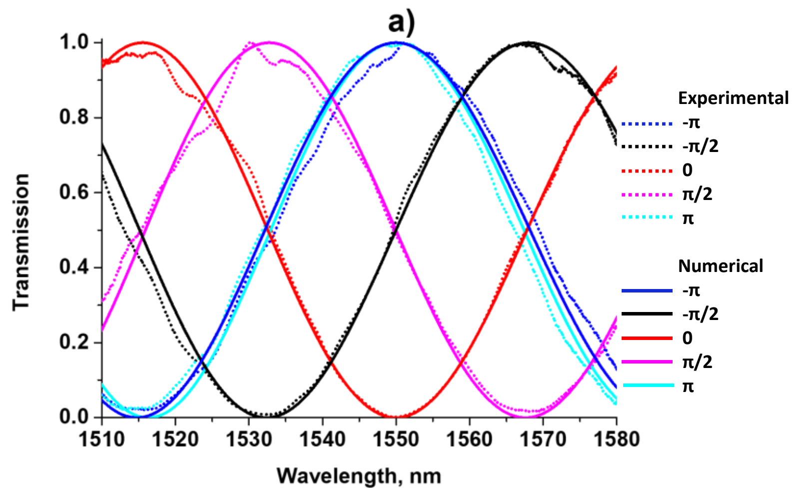

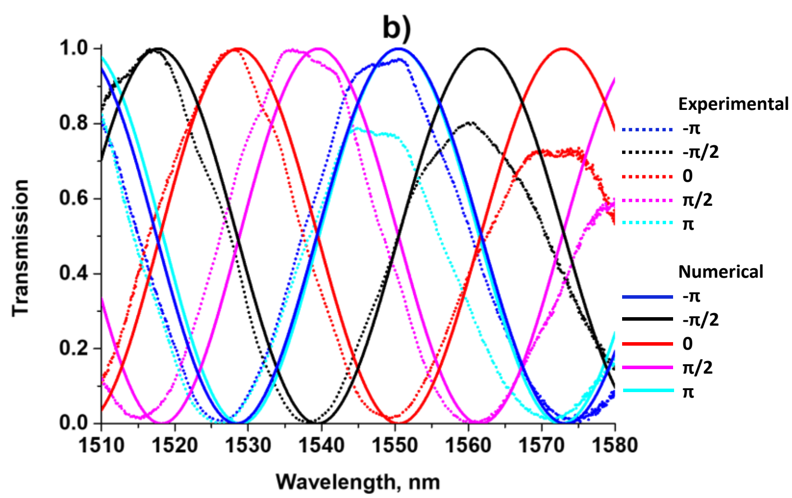

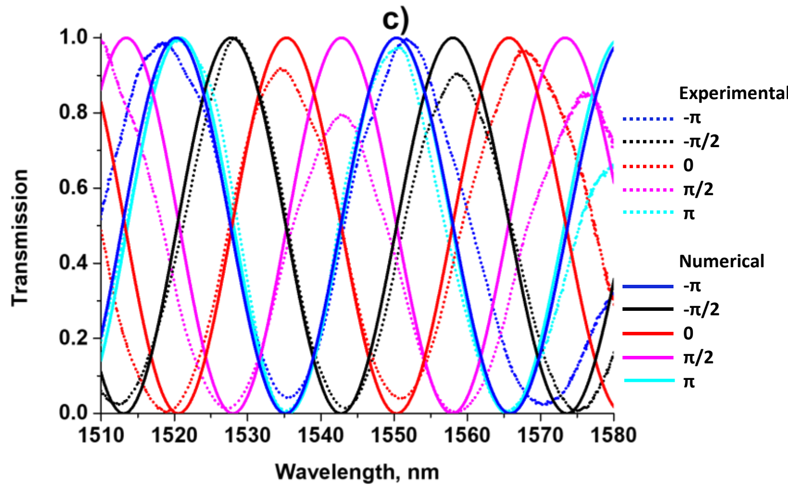

Fig. 5. LF transmission continuously tuned when changing δ_{l1} from $-\pi$ to π at 1550 nm by means of the VWR for a) 70 nm, b) 45 nm, and c) 30 nm periods, respectively. Experimental results: dotted lines and numerical results: solid lines.

Numerically, we follow the same procedure as in the experiment; first oriented the VWR at 90° and then increase δ_{l1} from 0 to π at 1550 nm (red, black and blue solid lines) so the spectrum blue-shifts and then to 0°, and increase δ_{l1} from 0 to π at 1550 nm (magenta and cyan solid lines) so the spectrum red-shifts. The results are plotted in Figs. 5a, 5b, and 5c for 70, 45, and 30 nm periods, respectively. These figures shows that the experimental measurements and the numerical simulations are also in agreement.

From the numerical results (solid lines), we calculate the experimental VWR retardance (squares) and plot it in Fig. 6. This figure shows that the wavelength shift slope depends on the LF period and increases with period. The corresponding slopes are 11.1408, 7.1619, and 4.7746 nm/rad for 70, 45, and 30 nm periods, respectively.

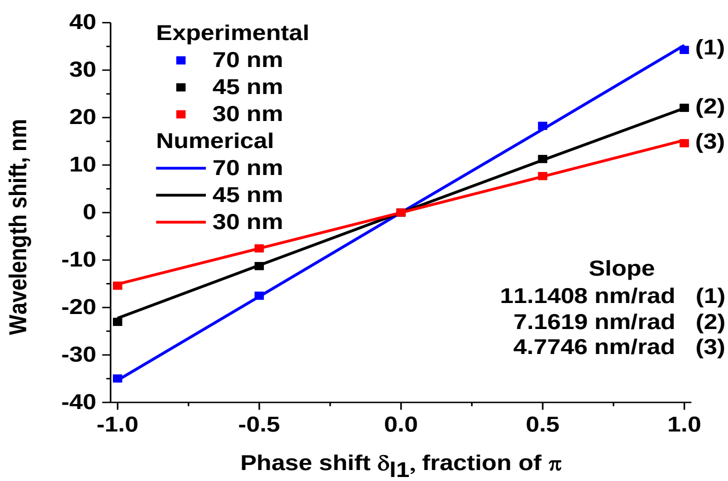

Fig. 6. LF wavelength shift for 70 nm (blue), 45 nm (black), and 30 nm (red) periods. Experimental results: squares, and numerical results: solid lines.

Finally, we change the modulation depth continuously from 0 to 1 by varying α_2 from 0° to -45° for $\varepsilon_z = 0$ (70 nm period). The experimental and numerical results are shown in Fig. 7a and Fig. 7b, respectively. Experimentally (Fig. 7a), it was possible to obtain modulation depths of 0.3403 (blue line), 0.4767 (black line), 0.6784 (red line), 0.8745 (magenta line), 0.9829 (cyan line), and 1 (green line) varying α_2 from 0° to -45° with 9° steps. Numerically (Fig. 7b), we vary α_2 as in the experiment with corresponding modulation depths of 0 (blue line), 0.3827 (black line), 0.7071 (red line), 0.9240 (magenta line), and 1 (cyan line), respectively. Figure 7c shows the experimental (red squares), and numerical (black line) modulation depths. As it can be seen, there is a small disagreement between the experimental and the numerical results that we attribute to a low rotator resolution (5°) and a small circular-induced birefringence by twisting splice 2 (α_2 from 0 to -45°) [28].

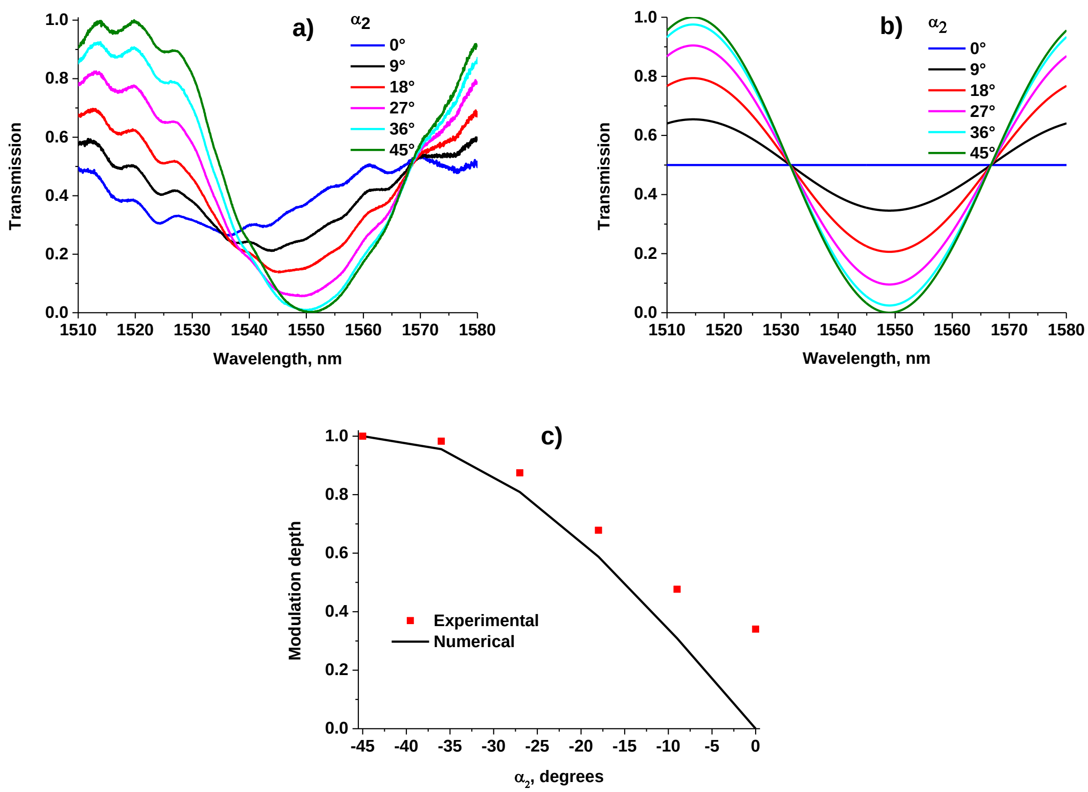

Fig. 7. a) Experimental and b) numerical LF transmission with modulation depth continuously changed from 0 to 1 by varying α_2 from 0° to -45° for $\varepsilon_z = 0$ (70 nm period). c) Modulation depth varying α_2 from 0° to -45° for experimental (red squares) and numerical results (black line).

4. Conclusions

In conclusion, we numerically and experimentally investigate an all-fiber fully controlled LF based on bend-induced linear birefringence with tension. By increasing the fiber strain, the filter period can be dynamically varied from 70 to 30 nm. Also, the LF can be continuously tuned by adjusting the retardance of a VWR and in modulation depth from 0 to 1 by varying the angle of an azimuth rotator. The experimental results were supported by numerical simulations.

Funding

Consejo Nacional de Ciencia y Tecnología, project 287315.

Acknowledgments

I. Armas-Rivera thanks Consejo Nacional de Ciencia y Tecnología postdoctoral fellow 3701567. L. A. Rodríguez-Morales thanks Consejo Nacional de Ciencia y Tecnología postdoctoral fellow 2482407.

Declaration of Competing Interest

The authors declare that they have no known competing financial interests or personal relationships that could have appeared to influence the work reported in this paper.

References

[1] M. E. Fermann and I. Hartl, Ultrafast fiber laser technology, IEEE J. Sel. Top. Quantum Electron. 15(1) (2009) 191-206, https://doi.org/10.1109/JSTQE.2008.2010246.
[2] B. Dong, D. P. Zhou and L. Wei, Temperature insensitive all-fiber compact polarization-maintaining photonic crystal fiber based interferometer and its applications in fiber sensors, J. Light. Technol. 28(7) (2010) 1011-1015, https://doi.org/10.1109/JLT.2009.2038802.
[3] Y. Wu, Y. Leng, J. Xi, and X. Li, Scanning all-fiber-optic endomicroscopy system for 3D nonlinear optical imaging of biological tissues, Opt. Express 17(10) (2009) 7907-7915, https://doi.org/10.1364/OE.17.007907.
[4] P. J. Winzer, D. T. Neilson, and A. R. Chraplyvy, Fiber-optic transmission and networking: the previous 20 and the next 20 years [Invited], Opt. Express 26(18) (2018) 24190-24239, https://doi.org/10.1364/OE.26.024190.
[5] L. Zhang, H. Jiang, X. Yang, W. Pan, S. Cui, and Y. Feng, Nearly-octave wavelength tuning of a continuous wave fiber laser, Sci. Rep. 7 (2017) 42611, https://doi.org/10.1038/srep42611.
[6] I. Armas-Rivera, L. A. Rodriguez-Morales, M. Durán-Sánchez, M. Avazpour, A. Carrascosa, E. Silvestre, E. A. Kuzin, M. V. Andrés, B. Ibarra-Escamilla, Wide wavelength-tunable passive mode-locked Erbium-doped fiber laser with a SESAM, Opt. Laser Technol. 134 (2021) 106593, https://doi.org/10.1016/j.optlastec.2020.106593.
[7] C. S. Goh, M. R. Mokhtar, S. A. Butler, S. Y. Set, K. Kikuchi and M. Ibsen, Wavelength tuning of fiber Bragg gratings over 90 nm using a simple tuning package, IEEE Photon. Technol. Lett. 15(4) (2003) 557-559, https://doi.org/10.1109/LPT.2003.809300.
[8] M. Johnson, Single-mode-fiber birefringent filters, Opt. Lett. 5(4) (1980) 142-144, https://doi.org/10.1364/OL.5.000142.
[9] R. M. Sova, C. Kim, and J. U. Kang, Tunable All-Fiber Birefringence Comb Filters, Optical Fiber Communications Conference 70 (2002) 698-699, https:/doi.org/10.1109/OFC.2002.1036657.
[10] P. S. Liang, Z. X, Zhang, Q. Q. Kuang, and M. H. Sang, All-fiber birefringent filter with fine tunability and changeable spacing, Laser Phys. 9 (2009) 2124-2128, https://doi.org/10.1134/S1054660X09210063.
[11] B. Lyot, Optical apparatus with wide field using interference of polarized light, C. R. Acad. Sci. Paris 197 (1933) 1593.
[12] K. Özgören and F. Ö. Ilday, All-fiber all-normal dispersion laser with a fiber-based Lyot filter, Opt. Lett. 35(8) (2010)1296-1298, https://doi.org/10.1364/OL.35.001296.
[13] W. Zou, Z. He, and K. Hotate, Complete discrimination of strain and temperature using Brillouin frequency shift and birefringence in a polarization-maintaining fiber, Opt. Express 17(3) (2009) 1248-1255, https://doi.org/10.1364/OE.17.001248.
[14] M. P. Fok, C. Shu, and W. Tang, A cascadable approach to produce widely selectable spectral spacing in birefringent comb filters, IEEE Photon. Technol. Lett, 18(18) (2006) 1937-1939, https://doi.org/10.1109/LPT.2006.882222.
[15] M. Wang, S. Fu, P. Shum, N. Q. Ngo, J. Wu and J. Lin, A tunable Lyot birefringent filter with variable channel spacing and wavelength using nonlinear polarization rotation in an SOA, IEEE Photon. Technol. Lett. 20(18) (2008) 1527-1529, https://doi.org/10.1109/LPT.2008.928832.
[16] Y. Zhu, F. Xiang, L. Jin, S. Y. Set and S. Yamashita, All-fiber dual-wavelength mode-locked laser using a bend-induced-birefringence Lyot-filter as gain-tilt equalizer, IEEE Photon. J. 11(6) (2019) 1-7, https://doi.org/10.1109/JPHOT.2019.2946380.

[17] Y. Zhu, Z. Cui, X. Sun, T. Shirahata, L. Jin, S. Yamashita, and S. Set, Fiber-based dynamically tunable Lyot filter for dual-wavelength and tunable single-wavelength mode-locking of fiber lasers, Opt. Express 28(19) (2020) 27250-27257, https://doi.org/10.1364/OE.402173.
[18] J. Ding, Z. Wen, B. Lu, K. Wang, H. Chen, and J. Bai, Wavelength switchable dissipative soliton mode-locked fiber laser based on Lyot filter, Opt. Laser Tecnhol. 144 (2021) 107460, https://doi.org/10.1016/j.optlastec.2021.107460.
[19] D. Han, L. Mei, Z. Hui, A. Soliman, K. Ren, Y. Zheng, T. Li, and J. Gong, Flexible wavelength-, pulse-controlled mode-locked all-fiber laser based on a fiber Lyot filter, Opt. Express 30 (23) (2022) 41271-41278, https://doi.org/10.1364/OE.473122.
[20] M. Dai, B. Liu, T. Shirahata, X. Sun, S. Yun Set, and S. Yamashita, All-polarization-maintaining, efficiently wavelength-tunable, Er-doped mode-locked fiber laser with a compact reflective Lyot filter Opt. Express 31 (17) (2023) 27810-27820, https://doi.org/10.1364/OE.495997.
[21] Z. Li, C. Wu, H. Dong, P. Shum, C.Y. Tian, S. Zhao, Stress distribution and induced birefringence analysis for pressure vector sensing based on single mode fibers, Opt. Express 16(6) (2008) 3955–3960, https://doi.org/10.1364/OE.16.003955.
[22] R. Ulrich, S. C. Rashleigh, and W. Eickhoff, Bending-induced birefringence in single-mode fibers, Opt. Lett. 5(6) (1980) 273-275, https://doi.org/10.1364/OL.5.000273.
[23] S. C. Rashleigh and R. Ulrich, High birefringence in tension-coiled single-mode fibers, Opt. Lett. 5 (8) (1980) 354-356, https://doi.org/10.1364/OL.5.000354.
[24] I. Armas-Rivera, L. A. Rodríguez-Morales, G. Beltrán-Pérez, M. Durán-Sánchez, B. Ibarra-Escamilla, Zero-order achromatic variable-wave retarder in standard single-mode optical fiber, Opt. Laser Technol, 148 (2022) 107754, https://doi.org/10.1016/j.optlastec.2021.107754.
[25] X. Roselló-Mechó, M. Delgado-Pinar, A. Díez, and M. V. Andrés, Measurement of Pockels' coefficients and demonstration of the anisotropy of the elasto-optic effect in optical fibers under axial strain, Opt. Lett. 41 (13) (2016) 2934-2937, https://doi.org/10.1364/OL.41.002934.
[26] L. A. Sánchez, A. Díez, J. L. Cruz, and M. V. Andrés, High accuracy measurement of Poisson's ratio of optical fibers and its temperature dependence using forward-stimulated Brillouin scattering, Opt. Express 30 (1) (2022) 42-52, https://doi.org/10.1364/OE.442295.
[27] S. -L. Tsao and W. -M. Cheng, Simplified Formula of Bending Loss for Optical Fiber Sensors, Fiber Integr. Opt. 21(5) (2002) 333-334, https://doi.org/10.1080/01468030290087723.
[28] R. Ulrich and A. Simon, Polarization optics of twisted single-mode fibers, Appl. Opt. 18 (13) (1979) 2241-2251, https://doi.org/10.1364/AO.18.002241.